

Y. Bazilevs · V. M. Calo · Y. Zhang · T. J. R. Hughes

Isogeometric fluid–structure interaction analysis with applications to arterial blood flow

Received: 29 March 2006 / Accepted: 5 April 2006 / Published online: 7 June 2006
© Springer-Verlag 2006

Abstract A NURBS (non-uniform rational B-splines)-based isogeometric fluid–structure interaction formulation, coupling incompressible fluids with non-linear elastic solids, and allowing for large structural displacements, is developed. This methodology, encompassing a very general class of applications, is applied to problems of arterial blood flow modeling and simulation. In addition, a set of procedures enabling the construction of analysis-suitable NURBS geometries directly from patient-specific imaging data is outlined. The approach is compared with representative benchmark problems, yielding very good results. Computation of a patient-specific abdominal aorta is also performed, giving qualitative agreement with computations by other researchers using similar models.

Keywords Isogeometric analysis · NURBS · Fluid–structure interaction · Vascular modeling · Navier–Stokes equations · Elastic arterial wall · Mesh movement · Blood flow

1 Introduction

Isogeometric analysis based on NURBS (non-uniform rational B-splines) was first introduced in [24] as an attempt to improve on and generalize the standard finite element method. Further study of isogeometric analysis showed that results superior to standard finite elements are obtained in the context of structural vibrations [7]. Mathematical analysis of the isogeometric approach was performed in [2]. Optimal approximation estimates in p , the polynomial order used to define NURBS functions, were obtained for h -refined meshes. Stability and optimal convergence was proved mathematically and verified numerically for problems of compressible and incompressible elasticity, Stokes flow, and

scalar advection–diffusion. In this paper, isogeometric analysis is applied to fluid–structure interaction (FSI) problems with particular emphasis on arterial modeling and blood flow. It is believed that the ability of NURBS to accurately represent smooth exact geometries, that are natural for arterial systems, but unattainable in the faceted finite element representation, and the high order of approximation of NURBS, should render fluid and structural computations more physiologically realistic.

Initial attempts to simulate blood flow in arteries made use of simplified geometries. This approach had limited applicability because of its inability to represent complex flow phenomena occurring in real blood vessels. The concept of patient-specific cardiovascular modeling was first established in [39], where real-life geometries were used to simulate blood flow. This opened the door for designing predictive tools for vascular modeling and treatment planning. Dramatic improvements in the computational results were observed in [39], yet the blood vessel wall was treated as being rigid. As was shown earlier, for example with the flexible and rigid wall computations [46–49], the rigid wall assumption precludes pressure wave propagation and overestimates wall shear stress. There exists a variety of methods to include the effect of the moving wall in computations, the most prevalent being the arbitrary Lagrangian–Eulerian (ALE) approach. For a general discussion of ALE, the reader is referred to [8–10, 22, 29] and references therein. Applications of ALE to hemodynamics are discussed in [12, 15, 16, 31] and references therein. Some of the other techniques include the coupled momentum method [14], the immersed finite element method [54], and the space-time finite element method [40–42].

This work adopts the ALE framework. The arterial wall is treated as a non-linear elastic solid in the Lagrangian description governed by the equations of elastodynamics. Blood is assumed to be a Newtonian viscous fluid governed by the incompressible Navier–Stokes equations written in the ALE form. The fluid velocity is set equal to the velocity of the solid at the fluid–solid interface. The coupled FSI problem is written in a variational form such that the stress compatibility

Y. Bazilevs · V. M. Calo · Y. Zhang · T. J. R. Hughes (✉)
Institute for Computational Engineering and Sciences,
The University of Texas at Austin, 201 East 24th Street, 1 University
Station C0200, Austin, TX 78712, USA
E-mail: hughes@ices.utexas.edu

condition at the fluid–solid interface is enforced weakly. The ALE equations require the specification of the fluid region motion. This motion is found by solving an auxiliary static linear-elastic boundary-value problem for which the fluid–solid boundary displacement acts as a Dirichlet boundary condition (see, e.g., [26]).

In Sect. 1 we formulate the FSI problem mathematically at the continuous level and give some discussion of spatial discretization and time integration. In Sect. 2 we give a brief review of the isogeometric analysis framework based on NURBS. In Sect. 3 we give an overview of patient-specific vascular model construction for use in NURBS-based isogeometric analysis. In Sect. 4 we present two benchmark problems and flow in a patient-specific abdominal aorta. In Sect. 5 we draw conclusions and give a summary of planned future work.

2 Formulation of the fluid–structure interaction problem

In this section we present the formulation of the FSI problem. We begin by introducing notation. Let $\Omega_0 \in \mathbb{R}^d$, $d = 2, 3$, open and bounded, be the initial or the reference configuration. Let $\Omega_t \in \mathbb{R}^d$, open and bounded, represent the current configuration, namely Ω_t is the image of Ω_0 under the motion $\mathbf{x} = \mathbf{x}(\mathbf{X}, t)$ with $\mathbf{X} \in \Omega_0$, and $t \in (0, T)$, the time interval of interest. In what follows, \mathbf{x} will be referred to as current coordinates, and \mathbf{X} as reference coordinates. Note that $\mathbf{x}(\mathbf{X}, 0) = \mathbf{X}$. The domain Ω_0 admits a decomposition

$$\Omega_0 = \Omega_0^f \cup \Omega_0^s, \quad (1)$$

where Ω_0^f is a subset of Ω_0 occupied by the fluid, and Ω_0^s is a subset of Ω_0 occupied by the solid. The decomposition is non-overlapping, that is

$$\Omega_0^f \cap \Omega_0^s = \emptyset. \quad (2)$$

Likewise,

$$\Omega_t = \Omega_t^f \cup \Omega_t^s, \quad (3)$$

with

$$\Omega_t^f \cap \Omega_t^s = \emptyset. \quad (4)$$

Let Γ_0^{fs} denote the boundary between the fluid and the solid regions in the initial configuration, and, analogously, let Γ_t^{fs} be its counterpart in the current configuration. The above setup is illustrated in Fig. 1. It is important to emphasize that the motion of the fluid domain is not the particle motion of the fluid. It does, however, conform to the particle motion of the arterial wall. That is, the Lagrangian description is adopted for the artery wall.

2.1 The fluid problem

In this section we give a weak formulation of the incompressible Navier–Stokes fluid in the ALE description. Let

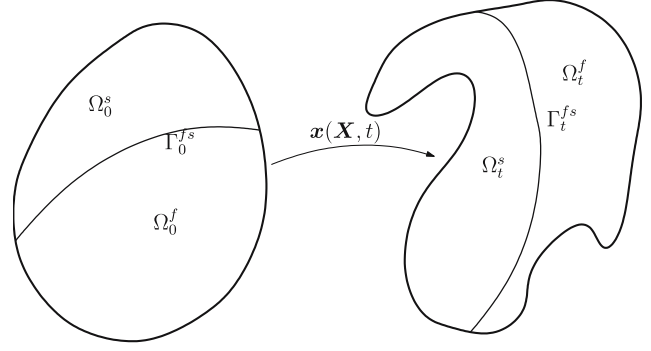


Fig. 1 Abstract setting for the fluid–structure interaction problem. Depiction of the initial and the current configurations related through the ALE mapping. The initial configuration also serves as the reference configuration

$\mathcal{V}^f = \mathcal{V}^f(\Omega_t^f)$ denote the trial solution space of velocities and pressures and let $\mathcal{W}^f = \mathcal{W}^f(\Omega_t^f)$ denote the trial weighting space for the momentum and continuity equations. Let $\{\mathbf{v}, p\}$ denote the particle velocity–pressure pair and $\{\mathbf{w}^f, q^f\}$ the weighting functions for the momentum and continuity equations. Let δ denote the displacement of the fluid region with respect to the initial configuration and $\partial\delta/\partial t$ be its velocity. Note that, unless the Lagrangian description is utilized in the fluid domain, $(\partial\delta/\partial t) \neq \mathbf{v}$. We also assume that the fluid particle velocity field satisfies the boundary condition, $\mathbf{v} = \mathbf{g}^f$ on $\Gamma_t^{f,D}$, the Dirichlet part of the fluid boundary. The variational formulation is stated as follows:

Find $\{\mathbf{v}, p\} \in \mathcal{V}^f$ such that $\forall \{\mathbf{w}^f, q^f\} \in \mathcal{W}^f$,

$$B^f \left(\{\mathbf{w}^f, q^f\}, \{\mathbf{v}, p\}; \frac{\partial\delta}{\partial t} \right) = F^f(\{\mathbf{w}^f, q^f\}), \quad (5)$$

where

$$\begin{aligned} B^f \left(\{\mathbf{w}^f, q^f\}, \{\mathbf{v}, p\}; \frac{\partial\delta}{\partial t} \right) = & \left(\mathbf{w}^f, \rho^f \frac{\partial\mathbf{v}}{\partial t} \right)_{\Omega_t^f} \\ & + \left(\mathbf{w}^f, \rho^f \left(\mathbf{v} - \frac{\partial\delta}{\partial t} \right) \cdot \nabla_x \mathbf{v} \right)_{\Omega_t^f} \\ & + (q^f, \nabla_x \cdot \mathbf{v})_{\Omega_t^f} \\ & - (\nabla_x \cdot \mathbf{w}^f, p)_{\Omega_t^f} \\ & + (\nabla_x^s \mathbf{w}^f, 2\mu^f \nabla_x^s \mathbf{v})_{\Omega_t^f}, \end{aligned} \quad (6)$$

and

$$F^f(\{\mathbf{w}^f, q^f\}) = (\mathbf{w}^f, \rho^f \mathbf{f}^f)_{\Omega_t^f} + (\mathbf{w}^f, \mathbf{h}^f)_{\Gamma_t^{f,N}}. \quad (7)$$

The above equations are written over the current configuration, and (\cdot, \cdot) defines the corresponding L^2 inner product. The subscript x on the partial derivative operators indicates that the derivatives are taken with respect to the current coordinates \mathbf{x} . $\Gamma_t^{f,N}$ is the Neumann part of the fluid domain boundary, \mathbf{h}^f is the boundary traction vector, \mathbf{f}^f is the body force per unit mass, and ρ^f and μ^f are the density and the dynamic viscosity of the fluid, respectively.

2.2 The solid problem

This section gives a weak formulation of the hyperelastic non-linear solid in the Lagrangian description. Let $\mathcal{V}^s = \mathcal{V}^s(\Omega_0^s)$ denote the trial solution space for displacements and let $\mathcal{W}^s = \mathcal{W}^s(\Omega_0^s)$ denote the trial weighting space for the linear momentum equations. Let \mathbf{u} denote the displacement of the solid body with respect to the initial configuration and let \mathbf{w}^s be the weighting function for the momentum equation. We also assume that the displacement satisfies the boundary condition, $\mathbf{u} = \mathbf{g}^s$ on $\Gamma_0^{s,D}$, the Dirichlet part of the solid domain boundary. The variational formulation is stated as follows:

Find $\mathbf{u} \in \mathcal{V}^s$ such that $\forall \mathbf{w}^s \in \mathcal{W}^s$,

$$B^s(\mathbf{w}^s, \mathbf{u}) = F^s(\mathbf{w}^s), \quad (8)$$

where

$$B^s(\mathbf{w}^s, \mathbf{u}) = \left(\mathbf{w}^s, \rho_0^s \frac{\partial^2 \mathbf{u}}{\partial t^2} \right)_{\Omega_0^s} + (\nabla_X \mathbf{w}^s, \mathbf{F} \mathbf{S})_{\Omega_0^s}, \quad (9)$$

and

$$F^s(\mathbf{w}^s) = (\mathbf{w}^s, \rho_0^s \mathbf{f}^s)_{\Omega_0^s} + (\mathbf{w}^s, \mathbf{h}^s)_{\Gamma_0^{s,N}}. \quad (10)$$

The above relations are written over the reference configuration. The subscript X on the partial derivative operators indicates that the derivatives are taken with respect to the material coordinates X . $\Gamma_0^{s,N}$ is the Neumann part of the solid boundary, \mathbf{h}^s is the boundary traction vector, ρ_0^s is the density of the solid in the initial configuration, and \mathbf{f}^s is the body force per unit mass. The displacement \mathbf{u} is defined as

$$\mathbf{u} = \mathbf{x} - \mathbf{X}, \quad (11)$$

\mathbf{F} is the deformation gradient

$$\mathbf{F} = \frac{\partial \mathbf{x}}{\partial \mathbf{X}} = \mathbf{I} + \frac{\partial \mathbf{u}}{\partial \mathbf{X}}, \quad (12)$$

and \mathbf{S} is the second Piola–Kirchhoff stress tensor. We consider the St. Venant–Kirchhoff constitutive relation:

$$\mathbf{S} = \mathcal{C} : \mathbf{E}, \quad (13)$$

where

$$\mathbf{E} = \frac{1}{2}(\mathbf{F}^T \mathbf{F} - \mathbf{I}), \quad (14)$$

$$\mathcal{C} = \lambda^s \mathbf{I} \otimes \mathbf{I} + 2\mu^s \left(\mathbb{I} - \frac{1}{3} \mathbf{I} \otimes \mathbf{I} \right), \quad (15)$$

$$\mathbb{I}_{ijkl} = \frac{1}{2}(\delta_{ik}\delta_{jl} + \delta_{il}\delta_{jk}), \quad (16)$$

\mathbf{E} is the Green–Lagrange strain tensor, δ_{ij} is the Kronecker delta, and λ^s and μ^s are the Lamé constants. Note that the fourth-order elastic tensor \mathcal{C} is assumed constant in this model.

The St. Venant–Kirchhoff model is not without shortcomings. It exhibits a seemingly spurious material instability under states of strong compression. However, this is not felt to be important in the present applications. The essential point is that it represents an objective generalization of the linear isotropic theory to the non-linear case. Of course, there is no physical justification of the model beyond the linear strain regime.

2.3 Motion of the fluid subdomain problem

This section gives a weak formulation of the motion of the fluid subdomain. Partial differential equations of linear elastostatics subject to Dirichlet boundary conditions coming from the displacements of the solid region define the ALE mapping $\mathbf{x}(\mathbf{X}, t)$ on the fluid domain. This construction, which is by no means unique, imposes sufficient regularity on the ALE mapping so as to make the fluid problem (5) well-posed. For precise conditions on the regularity of the ALE map, see Nobile [31]. In the discrete setting, the fluid subdomain motion problem is referred to as “mesh moving.”

Let $\mathcal{V}^m = \mathcal{V}^m(\Omega_t^f)$ denote the trial solution space of displacements and let $\mathcal{W}^m = \mathcal{W}^m(\Omega_t^f)$ denote the weighting space for the “elastic equilibrium” equations. Let δ denote the displacement of the fluid domain from its initial configuration and let \mathbf{w}^m be the weighting function for the linear momentum equations governing the motion of the fluid subdomain. Let $\Omega_{\tilde{t}}$ be the configuration of Ω_0 at $\tilde{t} < t$. We think of this as a “nearby” configuration that in numerical computations will typically represent the final configuration of the previous time step. Then, let $\tilde{\delta}$ be the displacement of the reference domain at time \tilde{t} . The variational formulation of the problem is stated as follows:

Find $\delta \in \mathcal{V}^m$ such that $\forall \mathbf{w}^m \in \mathcal{W}^m$,

$$B^m(\mathbf{w}^m, \delta) = 0, \quad (17)$$

subject to

$$\delta|_{\Gamma_t^{fs}} = \mathbf{u} \circ \mathbf{x}^{-1}|_{\Gamma_t^{fs}}, \quad (18)$$

and

$$\mathbf{w}^m|_{\Gamma_t^{fs}} = \mathbf{0}, \quad (19)$$

where

$$B^m(\mathbf{w}^m, \delta) = \left(\nabla_x^s \mathbf{w}^m, 2\mu^m \nabla_x^s (\delta - \tilde{\delta}) + \lambda^m \nabla_x \cdot (\delta - \tilde{\delta}) \right)_{\Omega_t^f}. \quad (20)$$

The above relations are written over the current configuration. The subscript x on the partial derivative operators indicates that the derivatives are taken with respect to the current coordinates \mathbf{x} . Constants μ^m and λ^m are the Lamé parameters of the linear elastic model characterizing the motion of the fluid region. Their choice at the continuous level should be such that the problem (17) is well-posed. In the discrete setting they should be selected such that the fluid mesh quality is preserved for as long as possible. In particular, mesh quality can be preserved by dividing the elastic coefficients by the Jacobian of the element mapping, effectively increasing the stiffness of the smaller elements [43], which are typically placed at fluid–solid interfaces. For advanced mesh moving techniques see [37, 38]. Parts of the boundary of the fluid region may also have motion prescribed to them independent of the motion of the solid region. This is handled in a standard way as a Dirichlet boundary condition. The remainder of the fluid region boundary is subjected to a “zero stress” boundary condition.

2.4 The coupled problem

In this section we present the coupled FSI problem, which is based on the individual subproblems introduced in previous sections of this paper. The variational formulation for the coupled problem is stated as:

Find $\{\mathbf{v}, p\} \in \mathcal{V}^f, \mathbf{u} \in \mathcal{V}^s$, and $\delta \in \mathcal{V}^m$ such that $\forall \{\mathbf{w}^f, q^f\} \in \mathcal{W}^f, \forall \mathbf{w}^s \in \mathcal{W}^s$, and $\forall \mathbf{w}^m \in \mathcal{W}^m$,

$$B^f\left(\{\mathbf{w}^f, q^f\}, \{\mathbf{v}, p\}; \frac{\partial \delta}{\partial t}\right) - F^f(\{\mathbf{w}^f, q^f\}) + B^s(\mathbf{w}^s, \mathbf{u}) - F^s(\mathbf{w}^s) + B^m(\mathbf{w}^m, \delta) = 0. \quad (21)$$

The following auxiliary relations hold in the sense of traces:

$$\mathbf{v}|_{\Gamma_t^{fs}} = \frac{\partial \mathbf{u}}{\partial t} \circ \mathbf{x}^{-1}|_{\Gamma_t^{fs}}, \quad (22)$$

$$\delta|_{\Gamma_t^{fs}} = \mathbf{u} \circ \mathbf{x}^{-1}|_{\Gamma_t^{fs}}, \quad (23)$$

$$\mathbf{w}^f|_{\Gamma_t^{fs}} = \mathbf{w}^s \circ \mathbf{x}^{-1}|_{\Gamma_t^{fs}}, \quad (24)$$

and

$$\mathbf{w}^m|_{\Gamma_t^{fs}} = \mathbf{0}. \quad (25)$$

Relationship (22), the kinematic constraint, equates the fluid velocity with that of the solid at the fluid–solid boundary. Equation (24) leads to the compatibility of stresses at the fluid–solid interface. Relations (23) and (25) indicate that the fluid region motion is driven by the displacement of the fluid–solid boundary acting as a Dirichlet boundary condition for the fluid motion subdomain problem.

Spatial discretization of the coupled problem (21) makes use of isogeometric analysis based on NURBS, an alternative approach to standard finite elements, proposed in Hughes et al. [24]. Isogeometric analysis is briefly reviewed in the next section. Galerkin's method is employed for the structural and the fluid subdomain motion parts of the formulation, while a residual-based multiscale method, given in Calo [5], and Hughes et al. [23], is used for the fluid equations. The class of residual-based multiscale methods may be thought of as stabilized methods, such as SUPG (see Brooks and Hughes [4]), extended to the non-linear realm.

The resultant semi-discrete equations are advanced in time using the generalized- α algorithm proposed by Chung and Hulbert [6] for the equations of structural mechanics and extended to the equations of fluid mechanics by Jansen et al. [25]. The generalized- α method embodies a family of second-order time integrators with strict control over high frequency dissipation. In the context of FSI, the generalized- α method was applied to the coupling of the linearized Euler equations with a non-linear structure in one spatial dimension by Kuhl et al. [28].

The kinematic constraint (22) is enforced strongly by requiring basis functions to be C^0 -continuous across the fluid–solid interface. Alternatively, this constraint may be enforced weakly by appropriately modifying the discrete formulation (see Bazilevs and Hughes [3]).

The coupled non-linear system is solved monolithically, that is, the fluid, the structural, and the mesh solution increments in the Newton iteration are obtained simultaneously. The effect of the structural and the mesh motion on the fluid equations is included in the left-hand-side matrix for robustness. The coupled system is solved iteratively by the GMRES procedure [34] with simple diagonal scaling. More sophisticated preconditioning strategies are under current investigation. For a description of different solution strategies for FSI equation systems see [44].

3 Isogeometric analysis and construction of vascular models

3.1 A brief review of isogeometric analysis employing NURBS

This section gives a very brief overview of isogeometric analysis based on NURBS. A more detailed description of the isogeometric approach may be found in [7, 24]. For an introductory text on NURBS, see Rogers [33], while a more detailed treatment is given in the book of Piegl and Tiller [32]. Mathematical theory of isogeometric analysis for h -refined meshes may be found in the recent work of Bazilevs et al. [2].

3.1.1 One-dimensional B-splines

A B-spline basis is comprised of piece-wise polynomials joined with prescribed continuity. In order to define a B-spline basis of polynomial order p in one dimension one needs the notion of a *knot vector*. A knot vector in one dimension is a set of coordinates in the parametric space, written as $\Xi = \{\xi_1, \xi_2, \dots, \xi_{n+p+1}\}$, where i is the knot index, $i = 1, 2, \dots, n + p + 1$, $\xi_i \in [0, 1]$ is the i th *knot*, and n is the total number of basis functions. A knot vector is said to be *open* if its first and last knots are repeated $p + 1$ times. Basis functions formed from an open knot vector are interpolatory at the end points of the parametric interval, but they are not, in general, interpolatory at the interior knots.

Given Ξ and p , B-spline basis functions are defined recursively starting with piecewise constants ($p = 0$):

$$B_{i,0}(\xi) = \begin{cases} 1 & \text{if } \xi_i \leq \xi < \xi_{i+1} \\ 0 & \text{otherwise} \end{cases}. \quad (26)$$

For $p = 1, 2, 3, \dots$, they are defined by

$$B_{i,p}(\xi) = \frac{\xi - \xi_i}{\xi_{i+p} - \xi_i} B_{i,p-1}(\xi) + \frac{\xi_{i+p+1} - \xi}{\xi_{i+p+1} - \xi_{i+1}} B_{i+1,p-1}(\xi). \quad (27)$$

Basis functions of order p have $p - 1$ continuous derivatives at knots. If a knot is repeated k times, then the number of continuous derivatives decreases by k . When the multiplicity of a knot is exactly p , the basis function is interpolatory. Basis functions form a partition of unity, each one is compactly supported on the interval $[\xi_i, \xi_{i+p+1}]$, and they are point-wise non-negative. These properties are important and make these functions attractive for use in analysis.

3.1.2 Multi-dimensional B-splines and geometrical objects

Let α be a positive integer such that $1 \leq \alpha \leq d$, where d is the number of space dimensions. Given α knot vectors Ξ_{γ, p_γ} , $\gamma = 1, \dots, \alpha$, multi-dimensional B-splines are constructed by taking tensor products of their one-dimensional counterparts:

$$B_{i_1, \dots, i_\alpha}(\xi_1, \dots, \xi_\alpha) = \otimes_{\gamma=1}^{\alpha} B_{i_\gamma, p_\gamma}(\xi_\gamma). \quad (28)$$

B-spline functions are defined on a parametric domain $(0, 1)^\alpha$, and p_γ is the polynomial order in the parametric direction γ .

Objects of B-spline geometry can be most generally characterized as unions of *patches* in \mathbb{R}^d . A patch is an image under a mapping of the parametric interval $(0, 1)^\alpha$, expressed as a linear combination of spline basis functions (28) and points in \mathbb{R}^d , that is,

$$\Omega = \{\mathbf{F}(\xi) | \xi \in (0, 1)^\alpha\}, \quad \mathbf{F}(\xi) = \sum_{i \in I} \mathbf{C}_i B_i(\xi), \quad (29)$$

where I is the index set

$$I = \{i = (i_1, \dots, i_\alpha) \in \mathbb{N}^\alpha \mid 1 \leq i_\gamma \leq n_\gamma + p_\gamma + 1\}, \quad (30)$$

Ω represents an object and the \mathbf{C}_i s are the so-called *control points*. Various geometrical objects may be obtained by varying α , namely: the case of $\alpha = 1$ corresponds to a *B-spline curve*, $\alpha = 2$ generates a *B-spline surface*, and a *B-spline solid* is obtained by setting $\alpha = 3$. A piece-wise linear interpolation of the control points for curves, and a piece-wise multi-linear interpolation of the control points for surfaces and solids is called a *control mesh*.

3.1.3 NURBS functions and geometry

The geometric framework based on B-splines is limited in that basic elements of engineering design, such as exact circles, ellipses, and other conic sections cannot be obtained by using B-spline functions alone. NURBS were devised to overcome this shortcoming. NURBS geometrical objects in \mathbb{R}^d are precisely *projective transformations* of B-spline geometrical objects in \mathbb{R}^{d+1} (see Farin [11]), that is,

$$\Omega = \{\mathbf{F}(\xi) \mid \xi \in (0, 1)^\alpha\},$$

$$\begin{aligned} \mathbf{F}(\xi) &= \mathcal{P} \left(\sum_{i \in I} \{\hat{\mathbf{C}}_i, w_i\} B_i(\xi) \right) \\ &= \sum_{i \in I} \left(\frac{\hat{\mathbf{C}}_i}{w_i} \right) \left(\frac{w_i B_i(\xi)}{\sum_{j \in I} w_j B_j(\xi)} \right) \\ &= \sum_{i \in I} \mathbf{C}_i \frac{w_i B_i(\xi)}{w(\xi)} = \sum_{i \in I} \mathbf{C}_i R_i(\xi). \end{aligned} \quad (31)$$

In the above $\hat{\mathbf{C}}_i$, \mathbf{C}_i are in \mathbb{R}^d , $w_i \in \mathbb{R}$, strictly positive, is the *weight*, and $w(\xi) = \sum_{i \in I} w_i B_i(\xi)$ is the *weighting function*. The weighting function is defined on the geometry and stays

unchanged throughout the refinement process. The last line of (31) defines NURBS basis functions $\{R_i\}_{i \in I}$:

$$R_i(\xi) = \frac{w_i B_i(\xi)}{w(\xi)}. \quad (32)$$

It is important to note that while a B-spline basis depends only on the structure of the knot vector, construction of a NURBS basis requires information about the geometry. Multi-dimensional NURBS basis functions are no longer tensor products of one-dimensional entities, in contrast with B-splines. Properties such as partition of unity, positivity, and compact support are retained for NURBS bases. Continuity of NURBS functions is also the same as that of B-splines.

3.1.4 Analysis framework based on NURBS

Isogeometric analysis framework consists of the following items and features:

1. A physical domain consists of a union of patches, each defined as an image of the parametric space as

$$\Omega = \{\mathbf{F}(\xi) \mid \xi \in (0, 1)^\alpha\}. \quad (33)$$

2. A mesh for a NURBS patch is defined by the union of NURBS elements, denoted by K , each one being an image under a NURBS map of a knot span in the parametric space

$$K = \{\mathbf{F}(\xi) \mid \xi \in \mathbf{Q} = \otimes_{\gamma=1}^{\alpha} (\xi_{i_\gamma, \gamma}, \xi_{i_\gamma + m_{i_\gamma, \gamma}})\}, \quad (34)$$

where m_{i_γ} is the multiplicity of knot $\xi_{i_\gamma, \gamma}$.

3. The basis for the solution space in the physical domain is defined through a composite mapping as follows:

$$N_i = R_i \circ \mathbf{F}^{-1}, \quad i \in I. \quad (35)$$

This definition gives the isoparametric construction [21], that is, the fields in question (e.g., displacement, velocity, temperature, etc.) are represented in terms of the same basis functions as the geometry. Coefficients of the basis functions, or *control variables*, are the degrees-of-freedom of the discrete system. The isoparametric approach is most convenient for applications involving Lagrangian and ALE descriptions of continuous media where geometry is constantly updated as the physical system evolves in time.

4. Boundaries of NURBS geometrical objects are themselves lower dimensions NURBS objects (e.g., a NURBS solid is bounded by NURBS surfaces, which, in turn, are bounded by NURBS curves). As a result, the easiest way to set Dirichlet boundary conditions on a patch face is to constrain control variables that correspond to that face. Interpolation or projection needs to be employed in cases when the prescribed function is not in the discrete space. This amounts to “strong” satisfaction of the boundary conditions. An alternative formulation of Dirichlet conditions can be based on “weak” satisfaction, a standard feature of the discontinuous Galerkin method. Neumann boundary conditions are satisfied as in the standard finite element method.

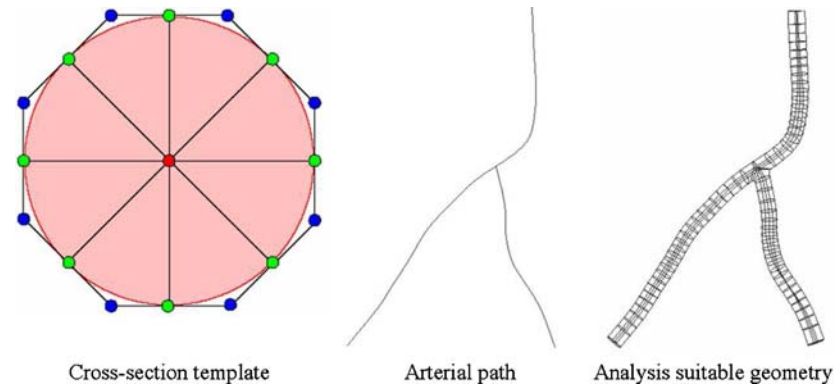


Fig. 2 Stages 3 and 4 of the patient-specific cardiovascular model construction for isogeometric analysis. *Left* Depiction of a cross-section surface template. Cross-section surface is bounded by a closed quadratic NURBS curve defined in terms of the control polygon consisting of 16 points. *Middle* Arterial path identified by skeletonization. *Right* Solid NURBS geometry, ready for refinement and analysis

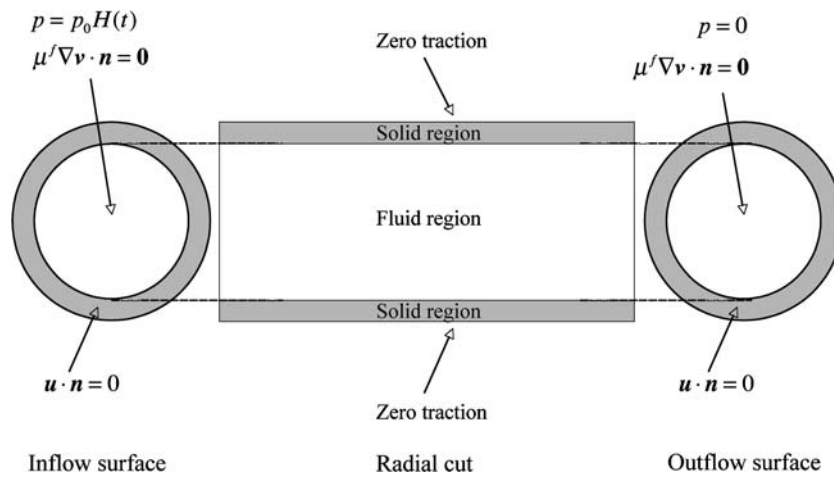


Fig. 3 Wave propagation in a fluid-filled elastic tube problem setup. $H(t)$ is the heaviside function

5. Mesh refinement strategies are developed from a combination of *knot insertion* and *order elevation* techniques. These enable analogues of classical *h*-refinement and *p*-refinement methods, and the new possibility of *k*-refinement. Details of refinement algorithms may be found in [24].

3.2 Construction of vascular models for isogeometric analysis

Construction of patient-specific models for isogeometric analysis is a process involving four stages, described below:

1. In scanned computed tomography (CT), or magnetic resonance imaging (MRI), of patient-specific data, intensity contrast may not be sufficiently sharp, images are often “noisy”, and the luminal surface is frequently blurred. As a result, preprocessing of the CT/MRI data is necessary to improve its quality. Techniques such as contrast enhancement [53], filtering [1], classification [45], and segmentation [52] are employed for this purpose.

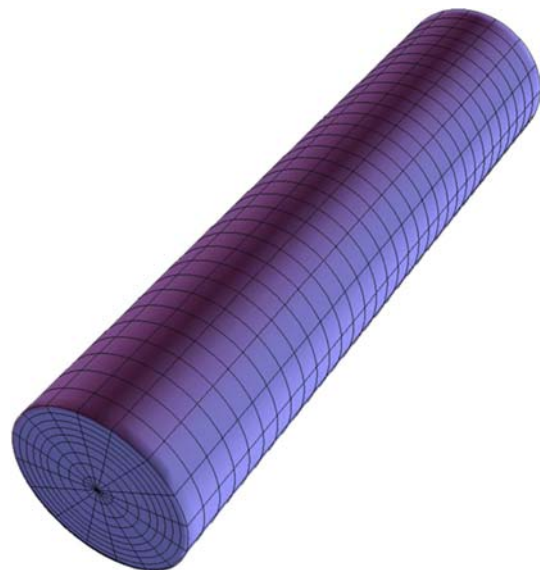


Fig. 4 Wave propagation in a fluid-filled elastic tube mesh consisting of 6,080 NURBS elements

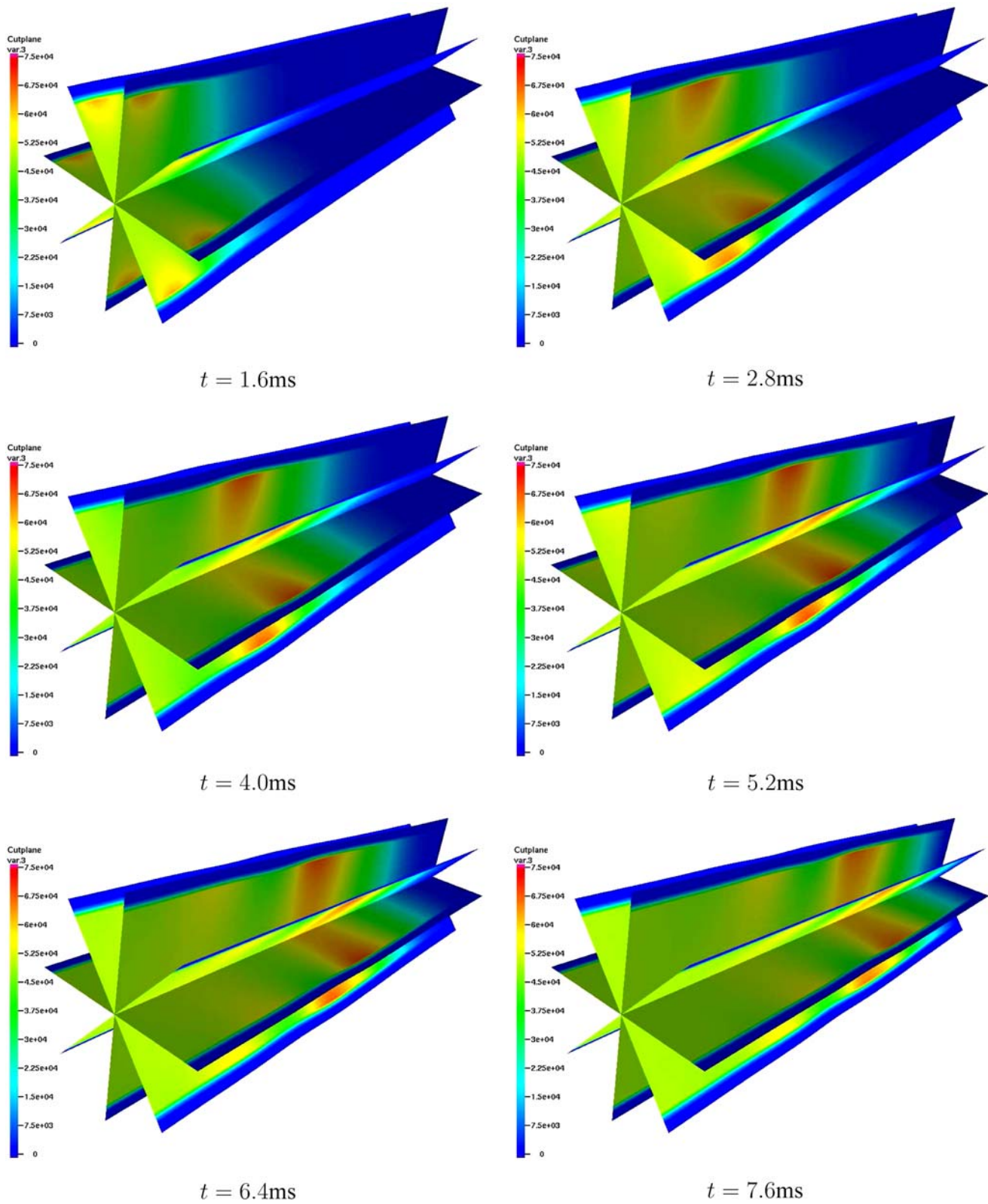


Fig. 5 Wave propagation in a fluid-filled elastic tube. Contours of fluid pressure at various radial slices. Solution remains point-wise axisymmetric

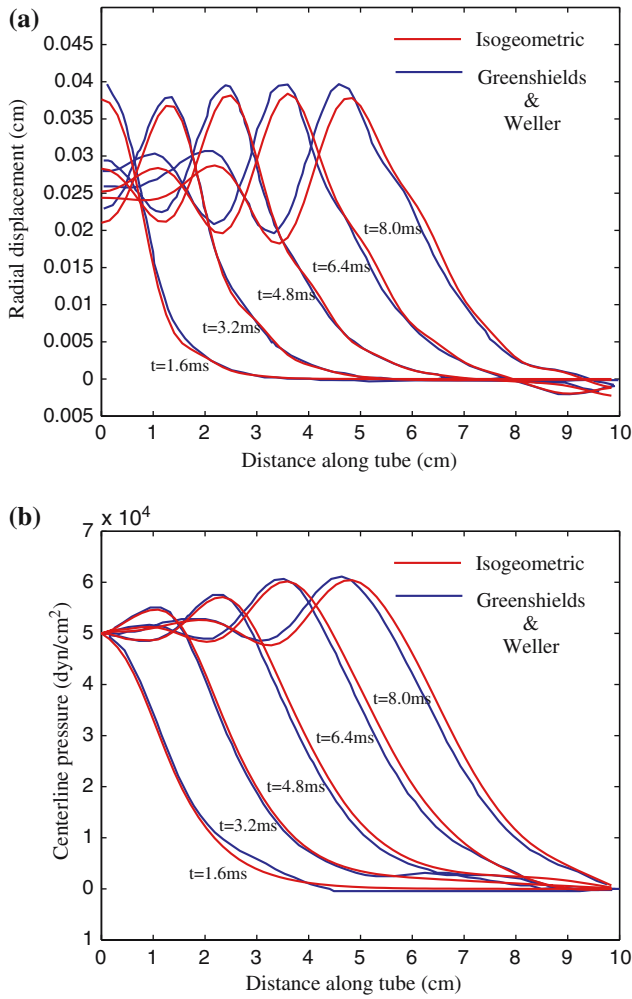


Fig. 6 Wave propagation in a fluid-filled elastic tube. **a** Outer wall radial displacement. **b** Centerline pressure. Computational results of Greenshields and Weller [18] are plotted for comparison

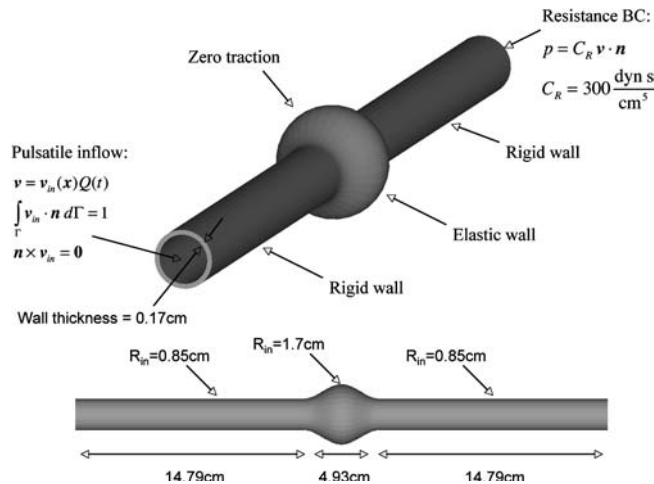


Fig. 7 Idealized aneurysm problem setup



Fig. 8 Idealized aneurysm mesh consisting of 14,630 NURBS elements

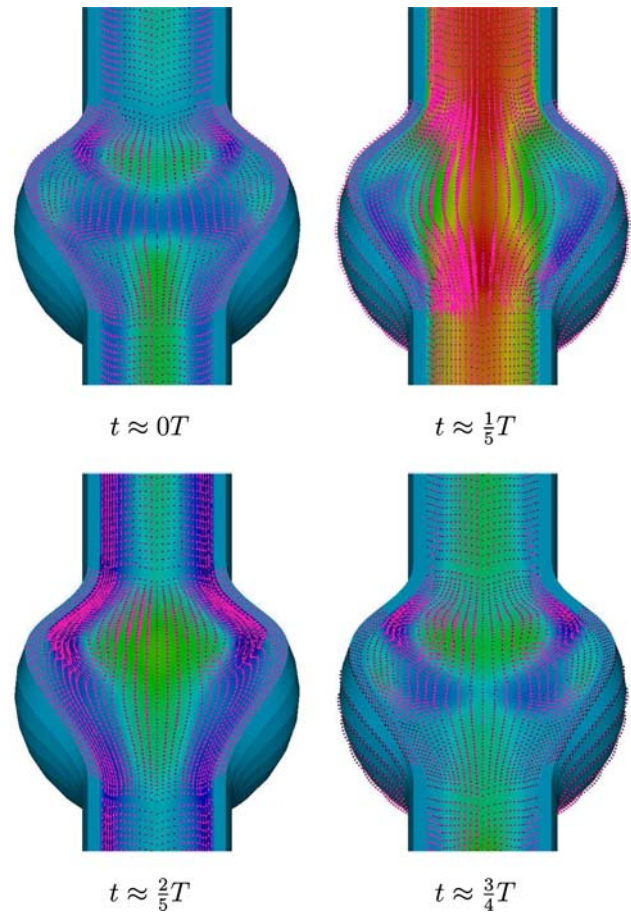


Fig. 9 Idealized aneurysm. Velocity vectors superimposed on axial velocity contours at various times. Top right and bottom left correspond to the systolic and diastolic phases, respectively. Note that the flow is axisymmetric despite the appearance of the figures. The apparent deviations from the axisymmetry are due to the plotting software utilized

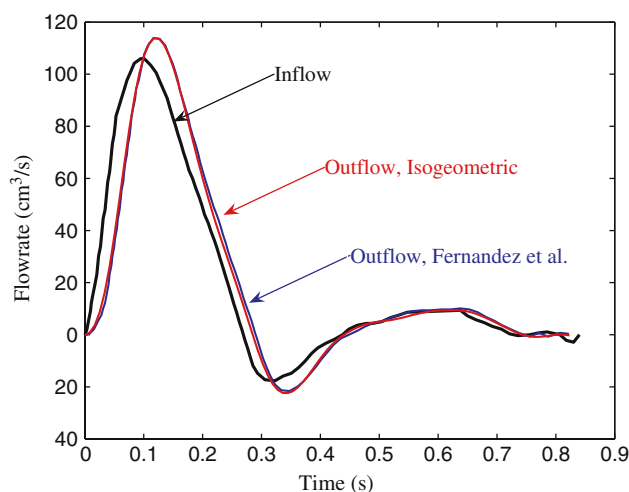


Fig. 10 Idealized aneurysm. Inflow and outflow waveforms. Notice the time lag attributable to the distensibility of the wall

2. The blood vessel surface model can then be constructed from preprocessed imaging data using isocontouring methods. The two main isocontouring methods, that make use of imaging data, are: primal contouring or marching cubes [30], and dual contouring [27]. The latter is chosen in this work for isosurface extraction, as it tends to generate surface meshes possessing better aspect ratios. In some cases geometric editing is required to remove unnecessary components and features. Once the luminal surface is identified, skeletonization technique [17] is employed in order to find paths.
3. We have developed a skeleton-based sweeping method to construct hexahedral NURBS control meshes for blood vessels [55]. The template faceted control polygon of a circle, projected onto the true surface, is swept along the arterial path to create a quadrilateral surface control mesh for a given arterial branch. Arterial branches are also arranged in a hierarchy, ranging from the largest to the smallest. Different cross-section templates are applied to different branches in the hierarchy. Templates for various branch intersections, such as bifurcations and trifurcations, are also worked out and applied on a case-by-case basis. See [55] for details.
4. Finally, solid NURBS meshes are constructed by filling in the volumes radially from the outer surface inward. Arterial wall meshes are obtained by extending the outer surface in the normal direction by a user-prescribed amount.

Stages 3 and 4 of the process are demonstrated on a simple example in Fig. 2.

4 Numerical examples

In all the examples, the wall is modeled by two elements and four C^1 -continuous second order basis functions through the thickness. See [24] for further details regarding modeling of shell-like structures as solids.

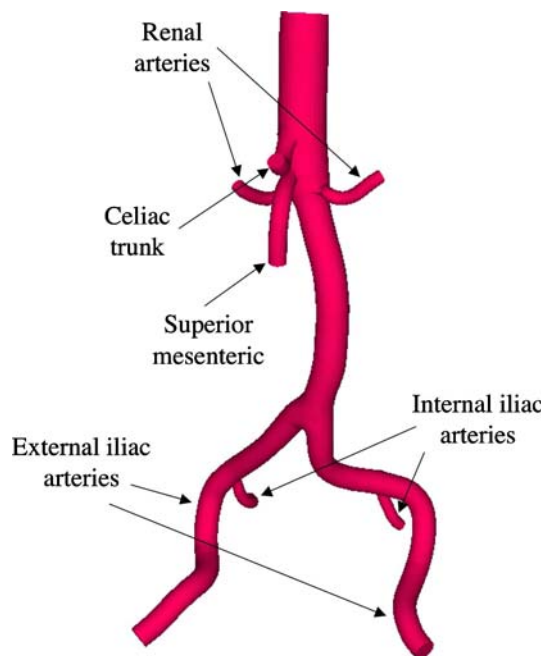


Fig. 11 Patient-specific abdominal aorta geometry



Fig. 12 Patient-specific abdominal aorta mesh consisting of 52,420 quadratic NURBS elements

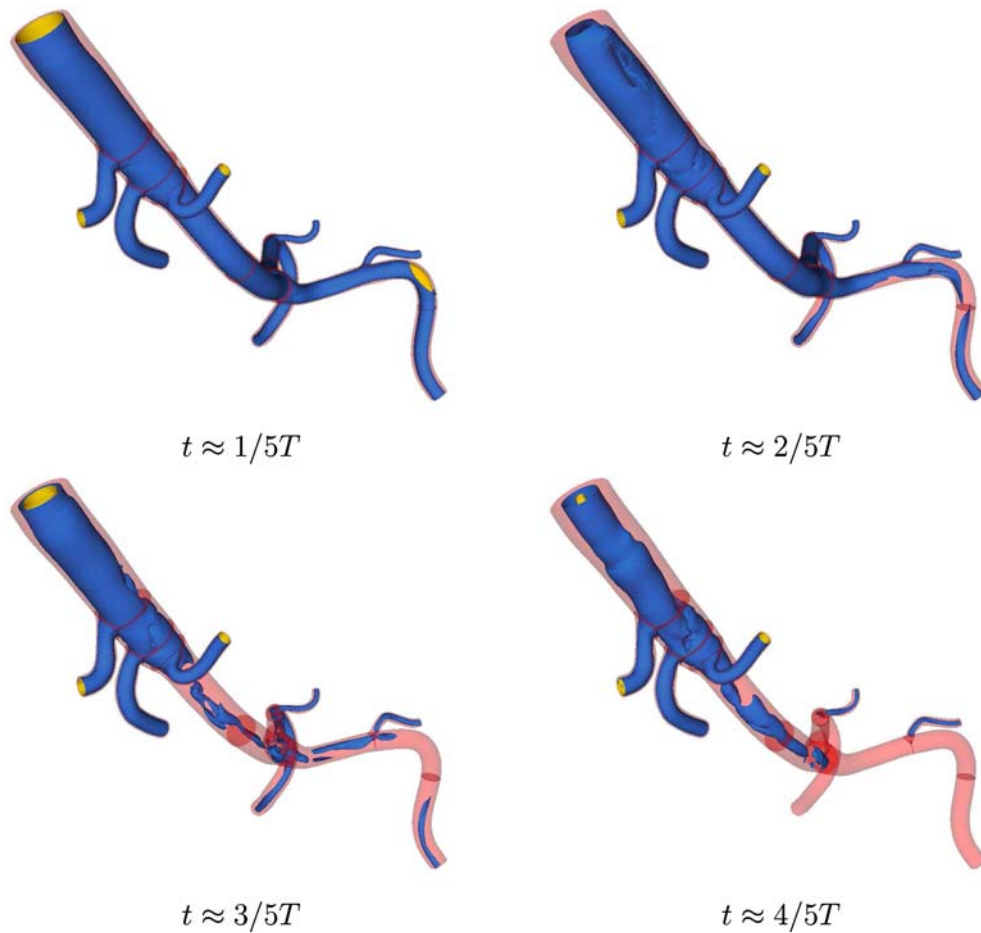


Fig. 13 Patient-specific abdominal aorta. Isosurfaces of the velocity magnitude plotted on the deformed geometry at various times

4.1 Wave propagation in an elastic tube

Our first test case, taken from Greenshields and Weller [18], deals with wave propagation in a fluid-filled elastic tube. In this example the tube length is $L = 10$ cm, its inner radius is $R_i = 1$ cm, and its outer radius is $R_o = 1.2$ cm. The solid region is enclosed between R_i and R_o while the fluid occupies the rest of the tube. The problem setup and boundary conditions are illustrated in Fig. 3. Material properties representative of blood flow in arteries are defined as follows: the density of the solid is $\rho^s = 1$ g/cm³, and Young's modulus and Poisson's ratio are $E = 10^7$ dyn/cm² and $\nu = 0.3$, respectively. The fluid density is also $\rho^f = 1$ g/cm³, and its viscosity is $\mu^f = 0.04$ g/cm s.

The computational mesh, consisting of 6,080 quadratic NURBS elements, is shown in Fig. 4. At $t = 0$ a step change in pressure is applied at the fluid inflow boundary to the system that is initially at rest (all initial fields are zero). The pulse causes a pressure wave to propagate down the tube. Figure 5 presents snapshots of fluid pressure at various times. Four radial cuts are shown on each of the plots to demonstrate that the computed solution is pointwise axisymmetric. For visualization purposes, pressure in the solid region is set to zero to create a sharp contrast at the fluid–solid interface. As a

result, radial wall displacement, which is on the order of 5%, is visible in the figure.

Figure 6a shows the outer wall displacement, while Fig. 6b shows the centerline fluid pressure at various times. Isogeometric results are compared with reference computations of Greenshields and Weller [18], who employed a small-strain, small-displacement formulation of the solid. Discrepancies between results are assumed attributable to the fully non-linear model used in the present study versus the linear model utilized in [18]. Nevertheless, results are in fairly good agreement with the reference computations, as well as with the Joukowsky solution (see Greenshields and Weller [18] for details). These observations provide tentative confirmation that the coupled momentum method for hemodynamics, proposed by Figueroa et al. [14], in which the fluid and the structure exhibit strong coupling, but the geometry stays fixed at a reference configuration, is an adequate description for blood flow calculations.

4.2 Blood flow in an idealized aneurysm

In this test case, taken from [13, 35], we examine pulsatile flow in an idealized aneurysm. The problem setup is shown

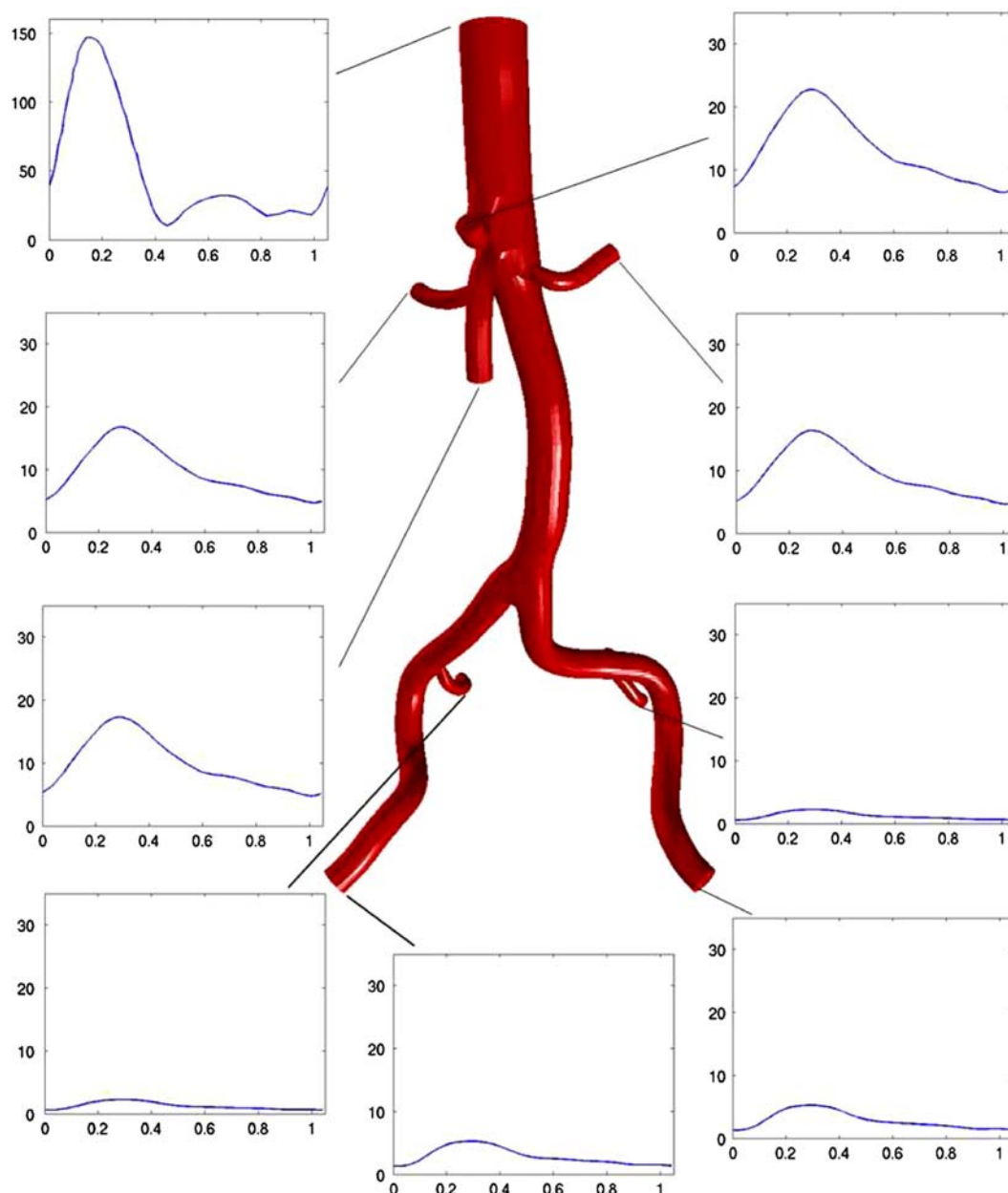


Fig. 14 Patient-specific abdominal aorta. Inlet and outlet flow waveforms. Flowrates (cm^3/s) versus time (s)

in Fig. 7. A time-periodic velocity waveform, specified at the inflow plane, is parabolically distributed over the circular surface. The period of the wave, T , is 0.84 s. The domains proximal and distal to the aneurysm region are assumed to have rigid walls, while the aneurysm wall is elastic. The density of the solid, its Young's modulus, and Poisson's ratio are $\rho^s = 1.2 \text{ g/cm}^3$, $E = 6 \times 10^6 \text{ dyn/cm}^2$, and $\nu = 0.3$, respectively. The fluid density and dynamic viscosity are $\rho^f = 1.012 \text{ g/cm}^3$ and $\mu^f = 0.035 \text{ g/cm s}$, respectively. A resistance boundary condition is applied at the outflow. The value of the resistance constant is $C_R = 300 \text{ dyn s/cm}^5$. For implementation of boundary conditions employing various pressure–flow relationships, see Heywood et al. [19] and

Vignon et al. [50]. The mesh, consisting of 14,630 quadratic NURBS elements, is shown in Fig. 8.

Figure 9 shows velocity vectors superimposed on the axial velocity contours in the aneurysm region at different times. A 135° “pie” slice was cut out of the domain in order to exhibit the flow features. Distensibility of the wall contributes significantly to the unsteadiness of the flow. Nevertheless, the flow remains axisymmetric, as may be discerned from symmetry of the velocity vectors. As in the previous example, no axisymmetry in the solution is assumed at the outlet. It should be noted that the peak Reynolds number, estimated to be about 1,400–1,500 based on the largest diameter, is close to the transitional value for circular pipe

flow (see, e.g., White [51]). Thus, relatively small perturbations in the geometry and/or flow conditions may lead to much more complex, unsteady solutions. Figure 10 shows the inflow and outflow waveforms. Note the outflow lags the inflow due to the distensibility of the aneurysm wall. This well-known phenomenon was also observed in the computations of Figueroa et al. [14]. Figure 10 also shows reference results from [13, 35]. The agreement is excellent despite the differences in the wall models (a non-linear shell was used in [13, 35]).

4.3 Patient-specific abdominal aorta

We present FSI calculations of a patient-specific abdominal aorta for a healthy over-55 volunteer obtained from 64-slice CT angiography. The geometrical model, which contains most major branches of a typical abdominal aorta, is shown in Fig. 11. The inferior mesenteric artery was not clearly captured in the imaging and was omitted in the geometrical model. The fluid properties are: $\rho^f = 1.06 \text{ g/cm}^3$, $\mu^f = 0.04 \text{ g/cm s}$. The solid is characterized by the density $\rho^s = 1 \text{ g/cm}^3$, Young's modulus, $E = 4.144 \times 10^6 \text{ dyn/cm}^2$, and Poisson's ratio, $\nu = 0.4$. A periodic flow waveform, with period $T = 1.05 \text{ s}$, is applied at the inlet of the aorta, while resistance boundary conditions are applied at all outlets. The solid is fixed at the inlet and at all outlets. Material and flow rate data, as well as resistance values are taken from Figueroa et al. [14], with the following exception. Poisson's ratio is taken to be 0.4, not 0.5 as in [14], as the latter is not allowed in the pure displacement formulation of an elastic solid. Wall thickness for this model is taken to be 15% of the nominal radius of each cross-section of the fluid domain model. The computational mesh, consisting of 52,420 quadratic NURBS elements, is shown in Fig. 12.

Figure 13 shows velocity isosurfaces plotted on the current configuration of the geometry at various times during the cardiac cycle. The flow appears to be fully three-dimensional and unsteady, with most of the unsteadiness occurring in late diastole. Figure 14 shows the distribution of flow among the branches. As in the previous example, the outflow lags the inflow due to the distensibility of the arterial wall. Although perfect matching with [14] cannot be expected because the geometry and analysis models are different, the overall flow distribution and the time lag are in qualitative agreement.

5 Conclusions and future work

We have developed a NURBS-based isogeometric FSI capability coupling incompressible fluids with non-linear elastic solids and allowing for large structural displacements, and applied it to problems of arterial blood flow. We have also developed a set of procedures allowing us to construct analysis-suitable NURBS geometries directly from patient-specific imaging data. The new approach is evaluated on two benchmark problems and applied to the FSI of a patient-specific abdominal aorta. Very good results are obtained for

the benchmark computations and the results for our patient-specific model are in qualitative agreement with the results of Figueroa et al. [14] for a patient-specific model.

Future developments will address extensions to hyperelastic materials with anisotropy and viscoelasticity (see, e.g., [20, 36]), which are capable of representing more physically realistic behavior of the arterial wall. Solid incompressibility and near-incompressibility will be dealt with by means of a mixed formulation employing displacement and pressure. Comparisons with standard finite elements are also planned.

Acknowledgments Y. Zhang was partially supported by the J.T. Oden ICES Postdoctoral Fellowship at the Institute for Computational Engineering and Sciences. This support is gratefully acknowledged. We would also like to thank Miguel Fernandez of INRIA for providing us with data for the idealized aneurysm as well as for his valuable comments and suggestions.

References

1. Bajaj C, Wu Q, Xu G (2003) Level set based volumetric anisotropic diffusion. ICES Report 03-10, UT Austin
2. Bazilevs Y, Beirão da Veiga L, Cottrell JA, Hughes TJR, Sangalli G (2006) Isogeometric analysis: approximation, stability and error estimates for h-refined meshes. *Math Models Methods Appl Sciences* (in press), available as ICES Report 06-04, UT Austin
3. Bazilevs Y, Hughes TJR (2006) Weak imposition of Dirichlet boundary conditions in fluid mechanics. *Comput Fluids* (In press), published online
4. Brooks AN, Hughes TJR (1982) Streamline upwind / Petrov–Galerkin formulations for convection dominated flows with particular emphasis on the incompressible Navier–Stokes equations. *Comput Methods Appl Mech Eng* 32:199–259
5. Calo VM (2004) Residual-based multiscale turbulence modeling: finite volume simulation of bypass transition. PhD thesis, Department of Civil and Environmental Engineering, Stanford University
6. Chung J, Hulbert GM (1993) A time integration algorithm for structural dynamics with improved numerical dissipation: the generalized- α method. *J Appl Mech* 60:371–75
7. Cottrell JA, Reali A, Bazilevs Y, Hughes TJR (2005) Isogeometric analysis of structural vibrations. *Comput Methods Appl Mech Eng* (In press), available as ICES Report 05-27, UT Austin
8. Donea J, Giuliani S, Halleux JP (1982) An arbitrary Lagrangian–Eulerian finite element method for transient dynamics fluid–structure interactions. *Comput Methods Appl Mech Eng* 33: 689–723
9. Farhat C, Geuzaine P (2004) Design and analysis of robust ALE time-integrators for the solution of unsteady flow problems on moving grids. *Comput Methods Appl Mech Eng* 193:4073–4095, 2004.
10. Farhat C, Geuzaine P, Grandmont C (2001) The discrete geometric conservation law and the nonlinear stability of ALE schemes for the solution of flow problems on moving grids. *J Comput Phys* 174(2):669–694
11. Farin GE (1995) *NURBS Curves and Surfaces: from Projective Geometry to Practical Use*. Peters AK, Natick
12. Fernandez MA, Moubachir M (2005) A Newton method using exact Jacobians for solving fluid–structure coupling. *Comput Struct* 83:127–142
13. Fernandez MA, Salsac A-V (2006) Numerical investigation of the effects of the wall compliance on the wall shear stress distribution in abdominal aortic aneurysms (in preparation)
14. Figueroa A, Vignon-Clementel IE, Jansen KE, Hughes TJR, Taylor CA (2005) A coupled momentum method for modeling blood flow in three-dimensional deformable arteries. *Comput Methods Appl Mech Eng* (in press)

15. Formaggia L, Gerbeau J-F, Nobile F, Quarteroni A (2001) On the coupling of 3D and 1D Navier–Stokes equations for flow problems in compliant vessels. *Comput Methods Appl Mech Eng* 191:561–582
16. Gerbeau J-F, Vidrascu M, Frey P (2005) Fluid-structure interaction in blood flows on geometries based on medical images. *Comput Struct* 83:155–165
17. Goswami S, Dey TK, Bajaj CL (2006) Identifying planar and cylindrical regions of a shape by unstable manifold 11th ACM Solid and Physical Modeling Symposium (to appear)
18. Greenshields CJ, Weller HG (2005) A unified formulation for continuum mechanics applied to fluid–structure interaction in flexible tubes. *Int J Numer Methods Eng* 64:1575–1593
19. Heywood JG, Rannacher R, Turek S (1996) Artificial boundaries and flux and pressure conditions for the incompressible Navier–Stokes equations. *Int J Numer Methods Fluids* 22:325–352
20. Holzapfel GA (2000) *Nonlinear solid mechanics, a continuum approach for engineering*. Wiley, Chichester
21. Hughes TJR (2000) *The finite element method: linear static and dynamic finite element analysis*. Dover, Mineola
22. Hughes TJR, Liu WK, Zimmermann TK (1981) Lagrangian–Eulerian finite element formulation for incompressible viscous flows. *Comput Methods Appl Mech Eng* 29:329–349
23. Hughes TJR, Calo VM, Scovazzi G (2004) Variational and multiscale methods in turbulence. In: Gutkowski W, Kowalewski TA, (eds) *Proceedings of the XXI international congress of theoretical and applied mechanics (IUTAM)*. Kluwer, New York
24. Hughes TJR, Cottrell JA, Bazilevs Y (2005) Isogeometric analysis: CAD, finite elements, NURBS, exact geometry, and mesh refinement. *Comput Methods Appl Mech Eng* 194:4135–4195
25. Jansen KE, Whiting CH, Hulbert GM (1999) A generalized- α method for integrating the filtered Navier–Stokes equations with a stabilized finite element method. *Comput Methods Appl Mech Eng* 190:305–319
26. Johnson AA, Tezduyar TE (1994) Mesh update strategies in parallel finite element computations of flow problems with moving boundaries and interfaces. *Comput Methods Appl Mech Eng* 119:73–94
27. Ju T, Losasso F, Schaefer S, Warren J (2002) Dual contouring of hermite data. In: *Proceedings of SIGGRAPH*, pp 339–346
28. Kuhl E, Hulshoff S, de Borst R (2003) An Arbitrary Lagrangian–Eulerian finite element approach for fluid–structure interaction phenomena. *Int J Numer Methods Eng* 57:117–142
29. Le Tallec P, Mouro J (2001) Fluid structure interaction with large structural displacements. *Comput Methods Appl Mech Eng* 190:3039–3068
30. Lorensen W, Cline H (1987) Marching cubes: a high resolution 3D surface construction algorithm. In: *SIGGRAPH*, pp 163–169
31. Nobile F (2001) *Numerical approximation of fluid–structure interaction problems with application to haemodynamics* PhD thesis, EPFL
32. Piegl L, Tiller W (1997) *The NURBS Book (Monographs in Visual Communication)*, 2nd edn. Springer, Berlin Heidelberg New York
33. Rogers DF (2001) *An Introduction to NURBS with Historical Perspective*. Academic, San Diego
34. Saad Y (1996) *Iterative Methods for Sparse Linear Systems*. PWS Albany
35. Salsas A-V, Fernandez MA, Chomaz J-M, Le Tallec P (2005) Effects of the flexibility of the arterial wall on the wall shear stress and wall tension in abdominal aortic aneurysms. In: *Proceedings of 58th annual meeting of the division of fluid dynamics*, Chicago November 2005
36. Simo JC, Hughes TJR (1998) *Computational Inelasticity*. Springer, Berlin Heidelberg New York
37. Stein K, Tezduyar T, Benney R (2003) Mesh moving techniques for fluid–structure interactions with large displacements. *J Appl Mech* 70:58–63
38. Stein K, Tezduyar TE, Benney R (2004) Automatic mesh update with the solid-extension mesh moving technique. *Comput Methods Appl Mech Eng* 193:2019–2032
39. Taylor CA, Hughes TJR, Zarins CK (1998) Finite element modeling of blood flow in arteries. *Comput Methods Appl Mech Eng* 158:155–196
40. Tezduyar TE, Behr M, Liou J (1992) New strategy for finite element computations involving moving boundaries and interfaces. The deforming-spatial-domain/space–time procedure. I. the concept and the preliminary numerical tests. *Comput Methods Appl Mech Eng* 94:339–351
41. Tezduyar TE, Behr M, Liou J (1992) New strategy for finite element computations involving moving boundaries and interfaces. The deforming-spatial-domain/space–time procedure. II. Computation of free-surface flows, two-liquid flows, and flows with drifting cylinders. *Comput Methods Appl Mech Eng* 94:353–371
42. Tezduyar TE (2003) Computation of moving boundaries and interfaces and stabilization parameters. *Int J Numer Methods Fluids* 43:555–575
43. Tezduyar TE, Behr M, Mittal S, Johnson AA (1992) Computation of unsteady incompressible flows with the stabilized finite element methods – space–time formulations, iterative strategies and massively parallel implementations. In: *New methods in transient analysis*, PVP-vol 246/ AMD-vol 143. ASME, New York: pp 7–24
44. Tezduyar TE, Sathe S, Keedy R, Stein K (2006) Space-time finite element techniques for computation of fluid–structure interactions. *Comput Methods Appl Mech Eng* 195:2002–2027
45. Tomasi C, Madcuchi R (1998) Bilateral filtering for gray and color images. In: *IEEE international conference on computer vision*, pp 839
46. Torii R, Oshima M, Kobayashi T, Takagi K, Tezduyar TE (2004) Influence of wall elasticity on image-based blood flow simulation. *Jpn Soc Mech Eng J Ser A* 70:1224–1231
47. Torii R, Oshima M, Kobayashi T, Takagi K, Tezduyar TE (2006) Computer modeling of cardiovascular fluid–structure interactions with the deforming-spatial-domain/stabilized space-time formulation. *Comput Methods Appl Mech Eng* 195:1885–1895
48. Torii R, Oshima M, Kobayashi T, Takagi K, Tezduyar TE (2006) Fluid–structure interaction modeling of aneurysmal conditions with high and normal blood pressures. *Comput Mech* (in press)
49. Torii R, Oshima M, Kobayashi T, Takagi K, Tezduyar TE (2006) Influence of the wall elasticity in patient-specific hemodynamic simulations. *Comput Fluids* (in press), published online
50. Vignon-Clementel IE, Figueroa CA, Jansen KE, Taylor CA (2005) Outflow boundary conditions for three-dimensional finite element modeling of blood flow and pressure in arteries. *Comput Methods Appl Mech Eng* (in press)
51. White F (1974) *Viscous Flow*. McGraw-Hill, New York
52. Yu Z, Bajaj C (2002) Image segmentation using gradient vector diffusion and region merging. In: *16th international conference on pattern recognition*, vol 2, pp 941–944
53. Yu Z, Bajaj C (2004) A fast and adaptive algorithm for image contrast enhancement. In: *IEEE international conference on image processing (ICIP'04)*, vol 2, pp 1001–1004
54. Zhang LT, Gerstenberger A, Wang X, Liu WK (2004) Immersed finite element method. *Comput Methods Appl Mech Eng* 193:2051–2067
55. Zhang Y, Bazilevs Y, Bajaj C, Hughes TJR (2006) Patient-specific vascular NURBS modeling for Isogeometric Analysis of blood flow. *ICES Report* 06–07